

Mathematical Basis and Validation of the Full Cavitation Model

Ashok K. Singhal

e-mail: aks@cfdr.com

Mahesh M. Athavale

Huiying Li

Yu Jiang

CFD Research Corporation,
Huntsville, AL 35805

Cavitating flows entail phase change and hence very large and steep density variations in the low pressure regions. These are also very sensitive to: (a) the formation and transport of vapor bubbles, (b) the turbulent fluctuations of pressure and velocity, and (c) the magnitude of noncondensable gases, which are dissolved or ingested in the operating liquid. The presented cavitation model accounts for all these first-order effects, and thus is named as the "full cavitation model." The phase-change rate expressions are derived from a reduced form of Rayleigh-Plesset equation for bubble dynamics. These rates depend upon local flow conditions (pressure, velocities, turbulence) as well as fluid properties (saturation pressure, densities, and surface tension). The rate expressions employ two empirical constants, which have been calibrated with experimental data covering a very wide range of flow conditions, and do not require adjustments for different problems. The model has been implemented in an advanced, commercial, general-purpose CFD code, CFD-ACE+. Final validation results are presented for flows over hydrofoils, submerged cylindrical bodies, and sharp-edged orifices. Suggestions for possible extensions of the model implementation, e.g., to nonisothermal flows, for ingestion and mixing of noncondensable gases, and for predictions of noise and surface damage are outlined.

[DOI: 10.1115/1.1486223]

Introduction

The capability for multidimensional simulation of cavitating flows is of critical importance for efficient design and performance of many engineering devices. Some examples are: industrial turbomachinery, turbopumps in rocket propulsion systems, hydrofoils, marine propellers, fuel injectors, hydrostatic bearings, and mechanical heart valves. In most cases, cavitation is an undesirable phenomenon, causing significant degradation in the performance, e.g., reduced flow rates, lower pressure increases in pumps, load asymmetry and vibrations and noise. Multidimensional simulations can enable a designer to eliminate, reduce or shift the cavitation regions. The objective of the present study is to develop a practical cavitation model capable of predicting major performance parameters. Its extensions to prediction of cavitation related surface damage, which affects the life of the equipment, may be considered in future.

Numerical simulation of cavitating flows poses unique challenges, both in modeling of the physics and in developing robust numerical methodology. The major difficulty arises due to the large density changes associated with phase change. For example, the ratio of liquid to vapor density for water at room temperature is over 40,000. Furthermore, the location, extent and type of cavitation are strongly dependent on the pressure field, which in turn is influenced by the flow geometry and conditions. Therefore, in a practical modeling approach, *a priori* prescription (or assumption) of the location and/or size of cavitation region should not be required. Likewise, the phase change correlations should have minimum essential empiricism so that diverse applications can be simulated without adjusting any constants or functions.

Over the last several decades, considerable effort from both experimental and analytical fronts has been devoted to understanding cavitation. For example, References [1–12] include some recent reviews as well as attempts on modeling and application of cavitation. Unfortunately, all past models, including the two de-

veloped by the principal author and his colleagues [10,11], have had limited success, primarily due to: (a) the lack of robustness of numerical algorithms, and (b) lack of generality of the correlations or approach used. As a result, no cavitation model was routinely used for practical CFD-based design optimization studies.

The Full Cavitation Model described here meets all the above-mentioned requirements and is already beginning to get routinely used in industry for water and oil pumps, inducers, impellers, and fuel injection systems.

Description of the Full Cavitation Model

The basic approach consists of using the standard viscous flow (Navier-Stokes) equations for variable fluid density and a conventional turbulence model (e.g., $k-\epsilon$ model). The fluid density is a function of vapor mass fraction f , which is computed by solving a transport equation coupled with the mass and momentum conservation equations. The $\rho-f$ relationship is:

$$\frac{1}{\rho} = \frac{f}{\rho_v} + \frac{1-f}{\rho_l} \quad (1)$$

and the vapor volume fraction α is deduced from f as:

$$\alpha \equiv f \frac{\rho}{\rho_v} \quad (2)$$

The vapor mass fraction, f , is governed by a transport equation:

$$\frac{\partial}{\partial t}(\rho f) + \nabla \cdot (\rho \vec{V} f) = \nabla \cdot (\Gamma \nabla f) + R_e - R_c \quad (3)$$

The source terms R_e and R_c denote vapor generation (evaporation) and condensation rates, and can be functions of: flow parameters (pressure, flow characteristic velocity) and fluid properties (liquid and vapor phase densities, saturation pressure, and liquid-vapor surface tension).

The above formulation employs a homogenous flow approach, also known as Equal-Velocity-Equal-Temperature (EVET) ap-

Contributed by the Fluids Engineering Division for publication in the JOURNAL OF FLUIDS ENGINEERING. Manuscript received by the Fluids Engineering Division April 20, 2001; revised manuscript received February 28, 2002. Associate Editor: J. Katz.

proach. For the objective of a practical and general model of cavitating flows, this is a fairly good simplification because of the following reasons:

1 In most engineering devices, the low-pressure regions, where cavitation occurs, are also the regions of relatively high velocities. In such high-velocity regions, the velocity slips between the liquid and vapor phases are rather small.

2 Most often, the generated vapor takes the form of small bubbles. While such flows can be characterized by a more rigorous two-fluid approach, which allows for velocity slip between the liquid and vapor phases, the computed flow fields strongly depend upon the physical models used for the computation of local bubble sizes and interface drag forces. Unfortunately, there are no general or reliable physical models for these parameters, and therefore the extra computational effort in the two-fluid approach is of little practical value.

The present model focuses on the use of simple rational formulations for phase change rates (R_e and R_c).

Bubble Dynamics Consideration. We assume that, in most engineering situations, there are plenty of nuclei for the inception of cavitation. Thus, our primary focus is on proper account of bubble growth and collapse. In a flowing liquid with zero velocity slip between the fluid and bubbles, the bubble dynamics equation can be derived from the generalized Rayleigh-Plesset equation as [1,12]:

$$\mathfrak{R}_B \frac{D^2 \mathfrak{R}_B}{Dt^2} + \frac{3}{2} \left(\frac{D \mathfrak{R}_B}{Dt} \right)^2 = \left(\frac{P_B - P}{\rho_l} \right) - \frac{4 \nu_l}{\mathfrak{R}_B} \frac{D \mathfrak{R}_B}{Dt} - \frac{2S}{\rho_l \mathfrak{R}_B} \quad (4)$$

This equation provides a physical approach to introduce the effects of bubble dynamics into the cavitation model. In fact, it can be considered to be an equation for void propagation and, hence, mixture density.

To obtain an expression of the net phase change rate, the two-phase continuity equations are written as follows: Liquid phase:

$$\frac{\partial}{\partial t} [(1 - \alpha) \rho_l] + \nabla \cdot [(1 - \alpha) \rho_l \vec{V}] = -R \quad (5)$$

Vapor phase:

$$\frac{\partial}{\partial t} (\alpha \rho_v) + \nabla \cdot (\alpha \rho_v \vec{V}) = R \quad (6)$$

Mixture:

$$\frac{\partial}{\partial t} (\rho) + \nabla \cdot (\rho \vec{V}) = 0 \quad (7)$$

where R is the net phase change rate ($R_e - R_c$), and ρ is the mixture density. Combining Eqs. (5)–(7) yields a relation between the mixture density and void fraction α :

$$\frac{D \rho}{Dt} = -(\rho_l - \rho_v) \frac{D \alpha}{Dt} \quad (8)$$

The vapor volume fraction α can be related to the bubble number density, “ n ” and radius of bubble \mathfrak{R}_B as

$$\alpha = n \frac{4}{3} \pi \mathfrak{R}_B^3 \quad (9)$$

substituting Eq. (9) into Eq. (8) we obtain

$$\frac{D \rho}{Dt} = -(\rho_l - \rho_v) (n 4 \pi)^{1/3} (3 \alpha)^{2/3} \frac{D \mathfrak{R}_B}{Dt} \quad (10)$$

Using the Rayleigh-Plesset Equation, Eq. (4), without the viscous damping and surface tension terms (the 2nd and 3rd term on r.h.s.), and combining Eqs. (5), (6), (8), and (10), the expression for the net phase change rate R is finally obtained as:

$$R = (n 4 \pi)^{1/3} (3 \alpha)^{2/3} \frac{\rho_v \rho_l}{\rho} \left[\frac{2}{3} \left(\frac{P_B - P}{\rho_l} \right) - \frac{2}{3} \mathfrak{R}_B \frac{D^2 \mathfrak{R}_B}{Dt^2} \right]^{1/2} \quad (11)$$

Using Eqs. (3) and (11), and ignoring the second-order derivative of \mathfrak{R}_B (important mainly during initial bubble acceleration), we get the following simplified equation for vapor transport:

$$\frac{\partial}{\partial t} (\rho f) + \nabla \cdot (\rho f \vec{V}) = (n 4 \pi)^{1/3} (3 \alpha)^{2/3} \frac{\rho_v \rho_l}{\rho} \left[\frac{2}{3} \left(\frac{P_B - P}{\rho_l} \right) \right]^{1/2} \quad (12)$$

where the right side of the equation represents the vapor generation or “evaporation” rate. Though we expect the bubble collapse process to be different from that of the bubble growth, as a first approximation, Eq. (12) is also used to model the collapse (condensation), when $P > P_B$, by using the absolute value of the pressure difference and treating the right side as a sink term. The local far-field pressure P is taken to be the same as the cell center pressure. The bubble pressure P_B is equal to the saturation vapor pressure in the absence of dissolved gas, mass transport and viscous damping, i.e., $P_B = P_v$.

Equation (12) is referred to here as the *Reduced Bubble Dynamics Formulation*.

Phase Change Rates. In Eq. (12), all terms except “ n ” are either known constants or dependent variables. In the absence of a general model for estimation of the number density, the Phase Change Rate expression is rewritten in terms of bubble radius, \mathfrak{R}_B , as follows:

$$R_e = \frac{3 \alpha}{\mathfrak{R}_B} \cdot \frac{\rho_v \rho_l}{\rho} \left[\frac{2}{3} \frac{P_v - P}{\rho_l} \right]^{1/2} \quad (13)$$

For simplicity, the typical bubble size \mathfrak{R}_B is taken to be the same as the limiting (maximum possible) bubble size. Then, \mathfrak{R}_B is determined by the balance between aerodynamic drag and surface tension forces. A commonly used correlation in the nuclear industry is [13]:

$$\mathfrak{R}_B = \frac{0.061 We \sigma}{2 \rho_l v_{rel}^2} \quad (14)$$

For bubbly flow regime, V_{rel} is generally fairly small, e.g., 5–10% of liquid velocity. By using various limiting arguments, e.g., $\mathfrak{R}_B \rightarrow 0$ as $\alpha \rightarrow 0$, and the fact that the per unit volume phase change rates should be proportional to the volume fractions of the donor phase, the following expressions for vapor generation/condensation rates are obtained in terms of the vapor mass fraction f :

$$R_e = C_e \frac{V_{ch}}{\sigma} \rho_l \rho_v \left[\frac{2}{3} \frac{P_v - P}{\rho_l} \right]^{1/2} (1 - f) \quad (15)$$

$$R_c = C_c \frac{V_{ch}}{\sigma} \rho_l \rho_l \left[\frac{2}{3} \frac{P - P_v}{\rho_l} \right]^{1/2} f \quad (16)$$

Here C_e and C_c are two empirical coefficients and V_{ch} is a characteristic velocity, which reflects the effect of the local relative velocity between liquid and vapor. These relations are based on the following assumptions:

1. In the bubble flow regime, the phase change rate is proportional to V_{rel}^2 ; however, in most practical two-phase flow conditions, the dependence on velocity is found/assumed to be linear.
2. The relative velocity between the liquid and vapor phase is of the order of 1 to 10% of the mean velocity. In most turbulent flows, the local turbulent velocity fluctuations are also of this order. Therefore, as a first pragmatic approximation, V_{ch} in Eqs. (15) and (16) can be expressed as the square root of local turbulent kinetic energy \sqrt{k} .

The Effect of Turbulence. Several experimental investigations have shown significant effect of turbulence on cavitating flows (e.g., references [3,14]). Also, Singhal et al. [11] reported a numerical model, using a probability density function (PDF) approach for accounting the effects of turbulent pressure fluctuations. This approach required: (a) estimation of the local values of the turbulent pressure fluctuations as [15]:

$$P'_{\text{turb}} = 0.39 \rho k \quad (17)$$

and (b) computations of time-averaged phase-change rates by integration of instantaneous rates in conjunction with assumed PDF for pressure variation with time. In the present model, this treatment has been simplified by simply raising the phase-change threshold pressure value as:

$$P_v = (P_{\text{sat}} + P'_{\text{turb}}/2) \quad (18)$$

This practice has been found to be much simpler, robust and almost as good as the more rigorous practice of ref. [11].

Effect of Noncondensable Gases (NCG). In most engineering equipment, the operating liquid contains a finite amount of non-condensable gas (NCG) in dissolved state, or due to leakage or by aeration. Even a small amount (e.g., 10 ppm) of NCG can have significant effects on the performance of the machinery [16,17]. The primary effect is due to the expansion of gas at low pressures which can lead to significant values of local gas volume fraction, and thus have considerable impact on density, velocity and pressure distributions. The secondary effect can be via increases in the phase-change threshold pressure. This has been neglected due to lack of a general correlation.

Final Form of Full Cavitation Model. The working fluid is assumed to be a mixture of liquid, liquid vapor and NCG. The calculation of the mixture density (Eq. (1)) is modified as:

$$\frac{1}{\rho} = \frac{f_v}{\rho_v} + \frac{f_g}{\rho_g} + \frac{1-f_v-f_g}{\rho_l} \quad (19)$$

Non-condensable gas density ρ_g is calculated as:

$$\rho_g = \frac{WP}{RT} \quad (20)$$

Volume fractions of NCG and liquid are modified as:

$$\alpha_g = f_g \frac{\rho}{\rho_g}; \quad (21)$$

$$\alpha_l = 1 - \alpha_v - \alpha_g \quad (22)$$

Finally, with the consideration of the NCG effect, and also using \sqrt{k} to replace V_{ch} , Eqs. (15) and (16) are rewritten as:

$$R_e = C_e \frac{\sqrt{k}}{\sigma} \rho_l \rho_v \left[\frac{2}{3} \frac{P_v - P}{\rho_l} \right]^{1/2} (1 - f_v - f_g) \quad (23)$$

$$R_c = C_c \frac{\sqrt{k}}{\sigma} \rho_l \rho_l \left[\frac{2}{3} \frac{P - P_v}{\rho} \right]^{1/2} f_v \quad (24)$$

where the phase-change threshold pressure P_v is estimated from Eqs. (17) and (18). The recommended values of the empirical constants C_e and C_c are 0.02 and 0.01, respectively. The basis for these values is described below.

Model Implementation

The full cavitation model has been implemented into an advanced, general purpose, commercial CFD code, CFD-ACE+ [18]. The relevant features of CFD-ACE+ include: unstructured/adaptive/hybrid grids, a finite volume, pressure-based formulation for incompressible and compressible flows, a variety of turbulence

models, multi-media heat transfer, steady-state and time-accurate solution, arbitrary sliding interface treatment, and moving grids for deforming/sliding domains.

Some points to be noted about the current cavitation model are:

1. The cavitation model can be applied to any geometric system (3D, 2D planar, or 2D axisymmetric); all grid cell types (quad, tri, hex, tet, prism, poly) and arbitrary interfaces are supported;
2. Concurrent use of the turbulence, grid deformation and/or structures solution modules are fully supported;
3. Flow is assumed isothermal and fluid properties are taken as constant at a given temperature for the entire flow domain. Due to this assumption, the cavitation module currently is decoupled from heat transfer and radiation modules.
4. Noncondensable gas mass fraction f_g is assumed to be constant in the flow field. An appropriate value of f_g , estimated based on the operating liquid and conditions, is prescribed as a part of the model input.

The simplifications listed in items 3 and 4 above can be removed in future as outlined at the end of the paper.

Determination of Empirical Constants C_e and C_c . The two constants, C_e and C_c , have been determined by performing several series of computations for sharp-edged orifice and hydrofoil flows. Both of these flows have excellent data, covering a wide range of operating conditions. Numerical computations were initially performed assuming $C_e = C_c$, and nominal values were found to be in the range 0.01–0.1. The assessment criteria included:

- (a) Comparison of computed mass flow rates, discharge coefficients, and flow pattern (location and extent of cavitation zone); and
- (b) Special attention to the calculated minimum pressures, and their sensitivity to the assumed values of coefficients.

The primary objectives of this exercise were to: completely eliminate negative pressure regions, obtain minimum pressures close to saturation pressures and obtain minimal sensitivity to pressure variations. It was found that to reproduce experimental trends, $C_c < C_e$. Several other postulations for slowing down the condensation (vapor destruction) process were also tried. None of these were found to be very general or robust. Therefore, C_c values were varied in the range of C_e to $0.1C_e$. A large number of combinations of C_e and C_c values were tried for several orifice flow conditions (upstream total pressure = 2, 3, 5, 50, and 500 bar) and for selected hydrofoil flow cases (representative low and high flow rates for two angles of attack, i.e., for leading and mid-chord cavitation). After many hundreds of permutations and combinations, the most satisfactory values were found to be

$$C_e = 0.02 \text{ and } C_c = 0.01 \quad (25)$$

These values were then used for many other problems, including flows past submerged cylindrical bodies, inducers, impellers and axial pumps. All these simulations produced satisfactory results, i.e., good convergence rates, no negative pressures, and reasonable comparison with available data and/or flow patterns. Therefore, the present set of values, $C_e = 0.02$ and $C_c = 0.01$ seems quite satisfactory for general use.

Validation of Full Cavitation Model

This section presents some of the validation results for flow over a hydrofoil, over a submerged cylindrical body, and flow in a sharp-edged orifice. In each case experimental data is available for wide range of conditions. Good agreement has been obtained in all cases without adjusting any coefficient values.

In all the simulations presented below, the working fluid was water at 300 K, with liquid and vapor densities of 1000 and 0.02558 kg/m³, saturation pressure of 3540 Pa and surface tension

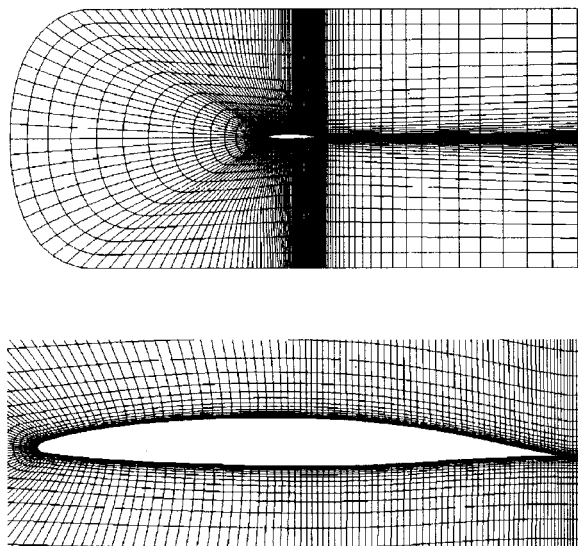


Fig. 1 Computational domain and grid, and grid distribution near the hydrofoil for $\alpha=4$ deg

$\sigma=0.0717$ N/m. A second-order upwind scheme was used to discretize the convective fluxes, and turbulence was treated using the standard k- ϵ model

1 Cavitating Flow Over a Hydrofoil. Effects of leading edge and mid-chord cavitation on the hydrodynamic forces on a hydrofoil were experimentally investigated by Shen and Dimotakis [19]. A NACA66 (MOD) airfoil section with camber ratio of 0.02, mean line of 0.8 and thickness ratio of 0.09 was used. A 2-D working section of the hydrofoil was mounted in a water tunnel. Static pressures on hydrofoil surface were measured at different angles of attack and Reynolds numbers. The non-dimensional parameters of interest were:

$$\text{Re} = \frac{\rho_l U_\infty C}{\mu_1}, \quad \Sigma = \frac{P_\infty - P_v}{\frac{1}{2} \rho_l U_\infty^2}, \quad C_p = \frac{P - P_\infty}{\frac{1}{2} \rho_l U_\infty^2} \quad (26)$$

A two-block grid consisting of 30×130 cells/block (7800 cells) is shown in Fig. 1. Two other grids consisting of 4250 and 14,700 cells were also used to check grid sensitivity of solutions. Calculated C_p values for the two higher cell count grids were found to differ less than 1%. Velocities, turbulence quantities and NCG mass fraction were specified at the left (inlet) boundary and an exit pressure was specified at the right (exit) boundary. The flow rate was varied to change the flow Reynolds number and the angle of attack was changed by airfoil section rotation. The NCG level was set to $f_g = 1$ ppm.

1.1 Leading Edge Cavitation. Simulations were performed at $\text{Re}=2 \times 10^6$ and an angle of attack of 4 deg; under these conditions, the cavitation is confined to the front of the hydrofoil. The exit pressure was varied to yield Σ values of 1.76, 1.0, 0.91 and 0.84. Calculated C_p values on hydrofoil top surface for two of the four cases are shown in Figs. 2 and 3 together with experimental data, and good correlation is seen. A typical vapor mass fraction distribution is shown in Fig. 4, which shows the cavitation zone on the hydrofoil surface.

1.2 Mid-Chord Cavitation. Simulations were performed at $\text{Re}=3 \times 10^6$ and an angle of attack of 1 deg. Cavitation inception was seen at $\Sigma=0.415$; simulations were performed at $\Sigma=0.43$, 0.38 and 0.34. Calculated and experimental plots of C_p on the hydrofoil top surface for two of the three cases are shown in Figs. 5 and 6. A cavitation zone exists in the mid-chord region and

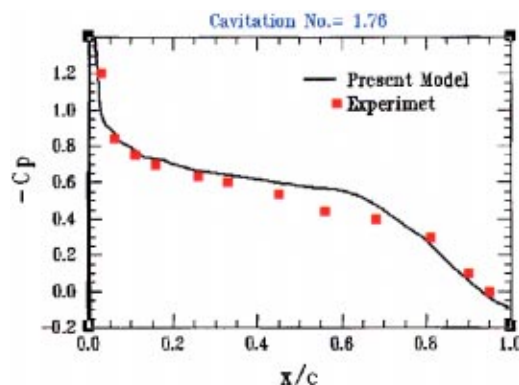


Fig. 2 Pressure variation on the suction side of a hydrofoil; $\Sigma=1.76$

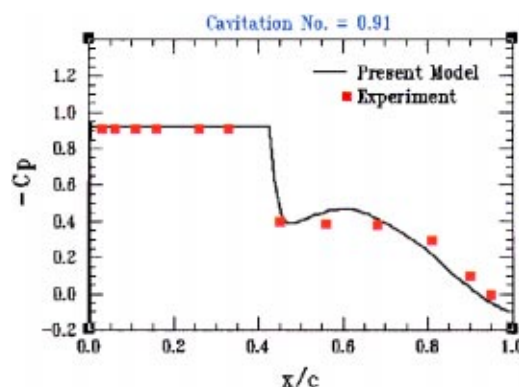


Fig. 3 Pressure variation on the suction side of a hydrofoil; $\Sigma=0.91$

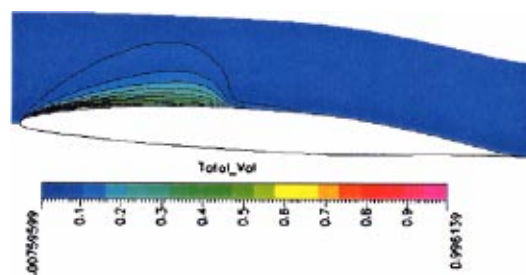


Fig. 4 Computed total volume fraction distributions at cavitation number=0.91

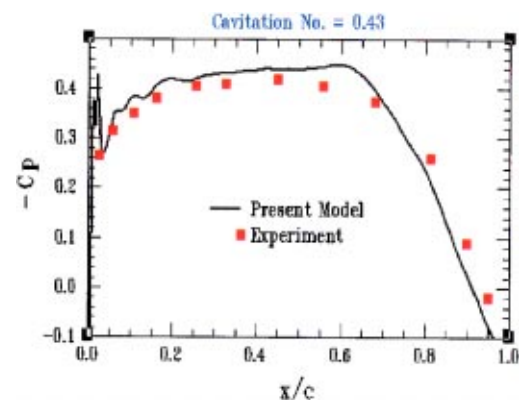


Fig. 5 Pressure variation on the suction side of a hydrofoil; $\Sigma=0.43$

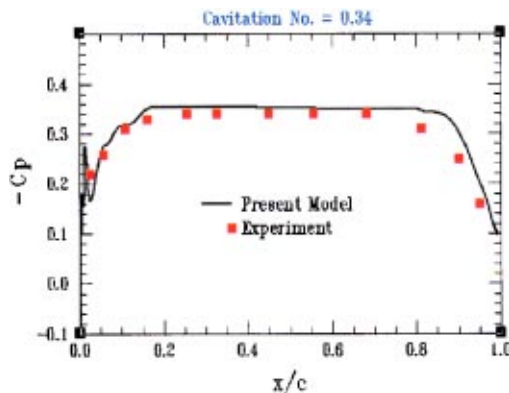


Fig. 6 Pressure variation on the suction side of a hydrofoil; $\Sigma=0.34$

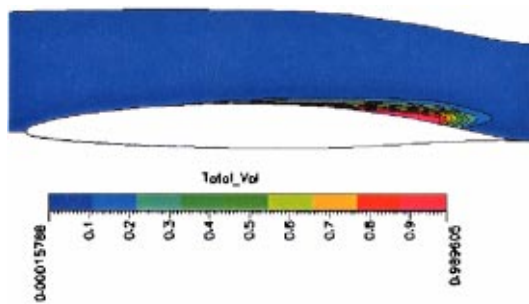


Fig. 7 Volume fractions for $\Sigma=0.34$, showing mid-chord cavitation

extends towards the trailing edge with decreasing Σ . A view of the cavitation zone for $\Sigma=0.34$ is shown in Fig. 7.

2 Front Cavitation Over Submerged Cylindrical Bodies

The present cavitation model was applied and assessed for cavitating flows over cylindrical submerged bodies with different types of head shapes. Extensive experimental data are reported by Rouse and McNown [20]. The experiments were conducted in a water tunnel with cylindrical test objects 0.025 m in diameter and 0.3048 m in length (1.0 in. and 12 in.). The flow was characterized using the parameters defined as:

$$\text{Re} = \frac{\rho_1 U_\infty d}{\mu_1}, \quad \Sigma = \frac{P_\infty - P_v}{0.5 \rho_1 U_\infty^2}, \quad C_p = \frac{P - P_\infty}{0.5 \rho_1 U_\infty^2} \quad (27)$$

2-D axisymmetric computational grids were built for these problems. All simulations were performed at a fixed inlet $U_\infty = 10$ m/s and exit pressure levels were varied to achieve the proper inlet pressure P_∞ . The NCG level was set to $f_g = 1$ ppm for the deaerated water used in the experiments. Computations were performed on bodies with hemispherical, 45 deg conical, and blunt heads. Details of the body with a 45 deg conical head are shown here.

The computational grid shown in Fig. 8 has two blocks with 61×39 and 124×39 cells (total of 7200 cells). Two other grids with 3375 and 12,700 cells were also used to check grid-independence of the solutions, and the C_p results for the two larger grids again differed by less than 1%. Results were obtained at $\Sigma = 0.3, 0.4, 0.5, 0.7, 1.0$ and 1.3 . Calculated and experimental distributions of C_p for four of the Σ values are shown in Fig. 9. Computed results match well with the experimental data. Pressure coefficients along the conical head, inside the cavitation zone and the recovery zone show very good agreement. Results for the other two cases (hemispherical and blunt heads) also showed similar agreements.

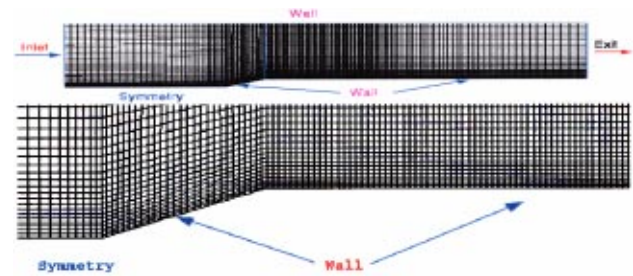


Fig. 8 Computational domain and grid, and grid distribution near a 45-degree conical fore-body

3 Cavitating Flow in a Sharp-Edged Orifice. Pressure-driven flow in a sharp-edged orifice is typically encountered in fuel-injectors, and has received a lot of attention. This is a very challenging flow computation, because the pressure differentials involved can be very high (up to 2500 bar), which drive a flow through a very small orifice, and the problem tests the robustness of the numerical and physical models.

Nurick [21] has published extensive experimental data for cavitation in a sharp-edged circular orifice. Geometrical parameters of the orifice are $D/d = 2.88$ and $L/d = 5$, where D , d , and L are inlet diameter, orifice diameter, and orifice length, respectively. Experiments were done with a fixed exit pressure, $P_b = 0.95$ bar, and the upstream total pressure, P_0 , was varied to generate different flow rates. High flow velocities near the orifice entrance generate a zone of very low pressure right after the constriction, where the flow cavitates. This reduces the flow rate (choking type phenomenon) and can lead to surface damage downstream of the orifice.

The discharge coefficient for the orifice, C_d , is of interest and the cavitation number Σ characterizes the flow:

$$\Sigma = \frac{P_o - P_v}{P_o - P_b}, \quad C_d = \frac{\dot{m}_{\text{actual}}}{\dot{m}_{\text{ideal}}} = \frac{\dot{m}_{\text{actual}}}{A_o \sqrt{2 \rho_1 (P_o - P_b)}} \quad (28)$$

$$C_d = C_c \sqrt{\Sigma} \quad (29)$$

where C_c , the contraction coefficient, was evaluated at 0.62.

The flow is 2-D axisymmetric, and a 2-block structured grid with 2800 cells (20×20 cells in the first block and 20×120 cells in the second) was employed to discretize the geometry with grid clustering around the sharp-edged corner (Fig. 10). The other grids used for grid sensitivity check had 1300 and 5400 cells. The predicted mass flow rates from the 2800 and 5400 cell grids varied by less than 1%. A large number of cases were computed, with the inlet total pressure ranging from 1.9 to 2500 bars; the inlet pressures and the corresponding cavitation numbers are listed in Table 1. NCG level f_g was set to 15 ppm.

Figure 11 shows the comparison between the predicted discharge coefficients C_d with Nurick's correlation, Eq. (29). The calculated values are in very close agreement with the experimental data. The model correctly predicts the inception of cavitation at $\Sigma = 1.7$. The discharge coefficient C_d is constant in the non-cavitating flow ($\Sigma > 1.7$), while it clearly shows a square-root dependence on Σ in the cavitation regime. The cavitation easily handles the flows at very low Σ values, where the upstream pressures are very high, over 2000 bar. Simulation of flows with such high pressure-ratios is a difficult task even for single-phase flow; but there were no difficulties in treating this flow with the full cavitation model, indicating the robustness of the numerical procedure.

Solution and Convergence Characteristics. In all the validation cases presented above, the computed minimum pressures are fairly close to the saturation pressures, and all error residuals drop by at least 4 orders of magnitude. Figures 12(a) and 12(b) show typical convergence plots for the hydrofoil and orifice cases

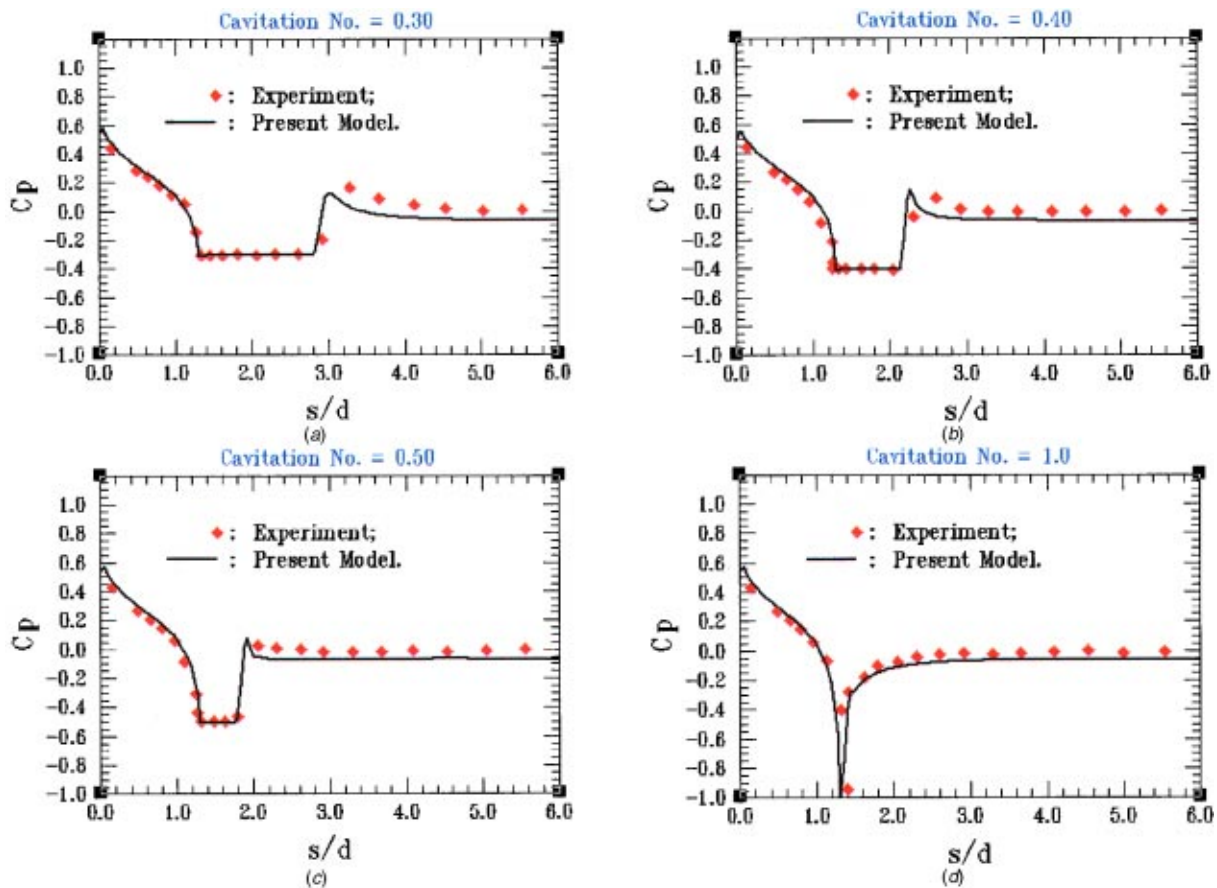


Fig. 9 Comparison between computed and measured C_p over a fore-body with a 45-degree conical head



Fig. 10 Computational grid used for the sharp-edged orifice

respectively. Convergence for the orifice case shows a plateau initially while the initial condition errors in the flow are convected out after which the solution converges rapidly.

Applications of the Full Cavitation Model

While the results presented here focused on the validation aspects of the cavitation model, this model has also been used successfully on a variety of different problems for research as well as commercial applications. These include:

1. Cavitation in diesel fuel injectors with complex multi-port geometries and time-varying geometries and pressure loading

Table 1 Total inlet pressure and cavitation number						
$P_o \times 10^5$ (Pa)	1.9	2.0	2.5	3.0	3.75	5.0
Σ	1.0004	1.001	1.009	1.019	1.101	1.226
$P_o \times 10^5$ (Pa)	10	50	100	500	1000	2500
Σ	1.327	1.446	1.590	1.704	1.871	1.963

2. Cavitation in rocket turbomachinery, e.g., cavitation in rocket inducers and impellers has been analyzed, and results validated against experiments. This work is being published separately [22,23].
3. Automotive Vane and Gear pump oil pump design optimization.
4. Cavitation in automotive thermostatic valves.

In all of these applications, the basic set of equations and constants described in previous sections have been found to generate accurate solutions with robust convergence characteristics.

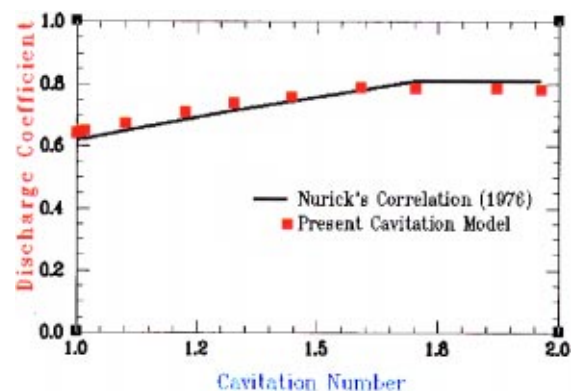
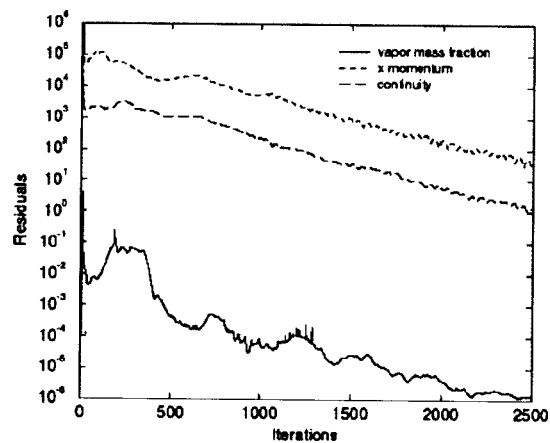
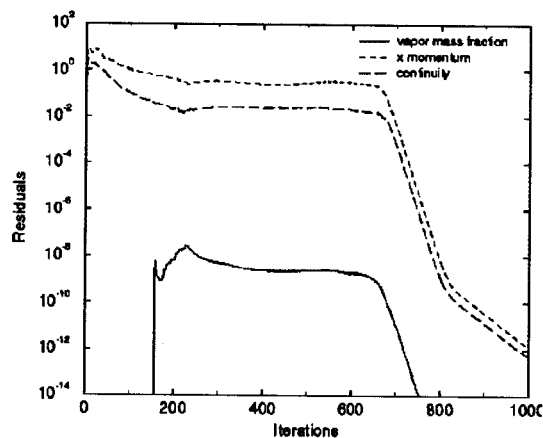


Fig. 11 Orifice cavitation: comparison of cavitation model predictions with Nurick's correlation



(a) *Hydrofoil, $\Sigma=0.34$*



(b) *Orifice, Upstream pressure=500 Bar*

Fig. 12 Convergence characteristics for two of the validation cases presented above; (a) hydrofoil, (b) orifice

Potential Extensions and Collaborations

The current limitations in the implementation of Full Cavitation Model in CFD-ACE+ include isothermal flow assumption, and a fixed, uniform mass concentration of NCG. Both of these assumptions can be easily relaxed by solving appropriate additional transport equation, and modifying corresponding parameters like P_{sat} and f_g . The present model provides many useful flow characteristics such as local gradients of pressure, density and volume fractions, general location and approximate extents of vapor regions, and approximate values of turbulence intensity. Approximate bubble size variations can also be deduced if desired. Since the model seems to be reasonably accurate for predictions of performance parameters over a wide range of conditions, it is very likely that the detailed flow characteristics are also in the realistic ranges. Such details can provide a sound foundation for the development of correlations for cavitation induced noise levels. A preliminary module based on integration of Lighthill equation using a Kirchhoff-Ffowacs-Williams-Hawking (KWFH) solver has already been developed and used on vane pump noise predictions. Likewise, appropriate additional equations and modules can be incorporated for the predictions of approximate location and magnitude of cavitation induced surface damage.

Because of the intricate inter-coupling of various physical models and numerical solution procedures and computer software data structures, the model extensions mentioned above will be best performed by universities and/or interested R&D groups working in close collaboration with the authors of the present paper.

Summary and Conclusions

A comprehensive model for cavitating flows has been developed and incorporated into an advanced CFD code for performance predictions of engineering equipment. This CFD code and cavitation model was applied to a number of validation and demonstration problems to verify the accuracy of the model and to assess the convergence performance on difficult engineering problems. Presented here were validation results for high-speed flow cavitation on hydrofoil and submerged cylindrical bodies, and in both cases the predictions from the cavitation model were in very good agreement with the experimental data. The model was also applied to cavitating flow through an orifice and computed results compared well with experimental data, even for very severe flow conditions involving very high pressure differentials across the orifice. The full cavitation model, coupled with CFD-ACE+ code, can be applied to a wide range of problems, and be a valuable prediction tool for design verification and optimization. Collaborative efforts are encouraged to extend this model, e.g., to include thermal effects and the prediction of cavitation damage.

Acknowledgments

This work was funded in part under NSF SBIR Grant No. DMI-9801239; this support is gratefully acknowledged. The authors would like to thank:

1. Dr. N. Vaidya and Ram Avva for their contributions in the development of two earlier models, which laid the basis for the current model; and
2. Mr. Dennis Gibson of Caterpillar, Inc., for his introduction and initial support for the development of cavitation model (even though it has taken over eight years to meet the challenge of developing a practical capability).

Nomenclature

C	= hydrofoil chord length
C_e, C_c	= constants in vapor generation condensation rate expression
D, d	= diameter
f_v, f_g	= vapor, gas mass fraction
k	= turbulence kinetic energy
m_{actual}	= actual orifice mass flow
m_{ideal}	= ideal orifice mass flow
n	= bubble number density
P	= pressure
P_v	= vapor pressure
P'_{turb}	= turbulence pressure fluctuation
Q	= flow rate
R	= universal gas constant
R_e, R_c	= vapor generation, condensation rates
Re	= Reynolds number
\mathcal{R}_B	= bubble radius
S	= surface tension
T	= temperature
U_∞	= freestream velocity
V	= fluid velocity vector
V_{ch}	= flow characteristic velocity
W	= molecular weight of non-condensable gas
We	= Weber number

Greek

α	= angle of attack
$\alpha_e, \alpha_v, \alpha_g$	= liquid, vapor, gas volume fraction
ρ, ρ_e, ρ_v	= density of mixture, liquid, vapor
σ	= surface tension
μ, ν	= dynamic, kinematic viscosities
Σ	= cavitation number

References

- [1] Kubota, A., Kato, H., and Yamaguchi, H., 1992, "A New Modeling of Cavitating Flows: A Numerical Study of Unsteady Cavitation on a Hydrofoil Section," *J. Fluid Mech.*, **240**, pp. 59–96.
- [2] Wang, Y.-C. and Brennen, C. E., 1994, "Shock Wave Development in the Collapse of a Cloud of Bubbles," *ASME FED*, Vol. 194, Cavitation and Multiphase Flow, pp. 15–19.
- [3] Keller, A. P., and Rott, H. K., 1997, "The Effect of Flow Turbulence on Cavitation Inception," *ASME FED Meeting*, Vancouver, Canada.
- [4] Janssens, M. E., Hulshoff, S. J., and Hoeijmakers, H. W. M., "Calculation of Unsteady Attached Cavitation," 28th AIAA Fluid Dynamics Conference, AIAA-97-1936.
- [5] Hsiao, C.-T., and Pauley, L. L., 1997, "Numerical Study of Tip Vortex Cavitation Inception Using a Bubble Dynamics Model," *ASME FED Meeting*, Vancouver, Canada.
- [6] Choi, J. K., and Kinnas, S. A., 1997, "Cavitating Propeller Analysis Inside of a Tunnel," *ASME FED Meeting*, Vancouver, Canada.
- [7] Fortes-Patella, R., and Reboud, J. L., 1998, "A New Approach to Evaluate the Cavitation Erosion Power," *ASME J. Fluids Eng.*, **120**, pp. 335–388.
- [8] Kunz, R. F., Boger, D. A., Chyczewski, T. S., Stinebring, D. R., Gibeling, H. J., and Govindan, T. R., 1999, "Multi-Phase CFD Analysis of Natural and Ventilated Cavitation about Submerged Bodies," *FEDSM99-3764*, *ASME Fluids Eng. Conf.*, San Francisco, CA.
- [9] Roth, K. W., and Massah, H., 1999, "Prediction of Cavitation Damage: A Comparison of Computational Fluid Dynamics and Experimental Results," *FEDSM99-6760*, *ASME Fluids Eng. Conf.*, San Francisco, CA.
- [10] Avva, R. K., Singhal, A. K., and Gibson, D. H., 1995, "An Enthalpy Based Model of Cavitation," *ASME FED Summer Meeting*, Hilton Head Island.
- [11] Singhal, A. K., Vaidya, N., and Leonard, A. D., 1997, "Multi-Dimensional Simulation of Cavitating Flows Using a PDF Model for Phase Change," *ASME FED Meeting*, Paper No. FEDSM'97-3272, Vancouver, Canada.
- [12] Brennen, C. E., 1995, *Cavitation and Bubble Dynamics*, Oxford University Press, Oxford.
- [13] Markatos, N. C., and Singhal, A. K., 1982, "Numerical Analysis of One-Dimensional, Two-Phase Flow a Vertical Cylindrical Pump," *Adv. Eng. Software*, **4**(3), pp. 99–106.
- [14] Stoffel, B., and Schuller, W., 1995, "Investigations Concerning the Influence of Pressure Distribution and Cavity Length on Hydrodynamic Cavitation Intensity," *ASME Fluids Eng. Conf.*, Hilton Head, SC.
- [15] Hinze, J. O., 1975, *Turbulence*, 2nd Ed. McGraw Hill, New York.
- [16] Watanabe, M., and Prosperetti, A., 1994, "The Effect of Gas Diffusion on the Nuclei Population Downstream of a Cavitation Zone," *ASME FED Vol. 190*, Cavitation and Gas Liquid Flow in Fluid Machinery and Devices.
- [17] Reisman, G., Duttweiler, and Brennen, C., 1997, "Effect of Air Injection on the Cloud Cavitation of a Hydrofoil," *ASME FED Meeting*, Vancouver, Canada.
- [18] CFDRC, 2001, "CFD-ACE+ Theory and Users' Manuals and Tutorials."
- [19] Shen, Y. J., and Dimotakis, P. E., 1989, "The Influence of Surface Cavitation on Hydrodynamic Forces," *Proc. 22nd ATTC*, St. Johns.
- [20] Rouse, H., and McNown, J. S., 1948, "Cavitation and Pressure Distribution, Head Forms at Zero Angle of Yaw," *Iowa Institute of Hydraulic Research*, Iowa City.
- [21] Nurick, W. H., 1976, "Orifice Cavitation and its Effect on Spray Mixing," *ASME J. Fluids Eng.*, **98**, pp. 681–687.
- [22] Athavale, M. M., Li, H. Y., Jiang, Y., and Singhal, A. K., 2000, "Application of the Full Cavitation Model to Pumps and Inducers," *ISROMAC-8*, Honolulu, HI.
- [23] Athavale, M. M., Li, H. Y., and Singhal, A. K., 2001, "Numerical Analysis of Cavitating Flows in Rocket Turbopump Elements," *Paper No. AIAA-2001-3400*.